This is a repository copy of *Structure:Function Relationships for Thermal and Light-Induced Spin-Crossover in Isomorphous Molecular Materials*.

White Rose Research Online URL for this paper:
https://eprints.whiterose.ac.uk/161210/

Version: Accepted Version

Structure:Function Relationships for Thermal and Light-Induced Spin-Crossover in Isomorphous Molecular Materials†‡

Rafal Kulmaczewski,[a] Elzbieta Trzop,[b] Eric Collet,[b,*] Sergi Vela[c,*] and Malcolm A. Halcrow[a,*]

Isomorphous [FeL_2][BF$_4$]$_2$·solv and [FeL_2][ClO$_4$]$_2$·solv (L = 4-{*iso*propylsulfanyl}-2,6-di{pyrazol-1-yl}pyridine; solv = MeNO$_2$, MeCN, 0.67Me$_2$CO or H$_2$O) exhibit a variety of thermal spin-crossover (SCO) behaviours. This complexity extends to the light induced excited spin state trapping (LIESST) experiment where, uniquely, five members show the expected inverse relationship between their thermal SCO ($T_{1/2}$) and LIESST relaxation (T(LIESST)) temperatures but a sixth compound ([FeL_2][BF$_4$]$_2$·MeCN) does not. The structural basis of these observations has been probed by X-ray crystallography, photocrystallography and periodic DFT+U+D2 calculations. Among the compounds examined, more cooperative thermal SCO is strongly coupled to order/disorder transitions in the solvent and/or *iso*propyl substituents and *vice versa*. A series of symmetry breaking phase transitions in [FeL_2][BF$_4$]$_2$·MeNO$_2$, before and after photoexcitation, occurs 10-20 K below T(LIESST) and has no direct bearing on the $T_{1/2}/T$(LIESST) relationship. These phase changes are not shown by other compounds in the study. The anomalous T(LIESST) in [FeL_2][BF$_4$]$_2$·MeCN, and its observed negative lattice expansion during isothermal low→high-spin conversion, are not reproduced computationally which implies those properties are unconnected to its spin state energetics. Its minimised high- and low-spin structures also deviate more from experiment than the other compounds investigated, in the most plastic region of the lattice which includes the solvent molecule. We conclude that reorientation of the linear MeCN molecule contributes a temperature-dependent lattice activation barrier to the spin-transition in [FeL_2][BF$_4$]$_2$·MeCN, leading to the higher T(LIESST) value observed.

Introduction

Spin-crossover (SCO) compounds undergo a spin state transition during a change in temperature, or other physical or chemical stimuli.[1-4] This is accompanied by a change in magnetic moment, and often by a colour change;[5] materials showing switchable conductivity,[6] fluorescence,[7] dielectric,[8,9] mesogenic[9,10] and mechanical properties[11] mediated by SCO have also been designed. While SCO can occur in any phase of matter, the crystal engineering of SCO molecular materials is of particular current interest.[12] Optimisation of SCO materials as switching centres in nano- or macro-scale devices,[3,11,13] as reporters for sensor applications[14] or as solid state coolants[15] will benefit from the design of new materials with bespoke switching properties.[16] More generally, SCO crystals are also useful testbeds for mechanistic studies of crystallographic phase changes and other solid state dynamics.[17]

Triggering SCO at low temperatures in solid materials can trap the samples in their excited high-spin state. This is termed Light-Induced Excited Spin State Trapping (LIESST), when the low→ high spin excitation is done photochemically.[18] The sample cannot relax to its low-spin ground state until it is warmed sufficiently for its lattice dynamics to accommodate the structural changes associated with the spin state change. The temperature of this relaxation, T(LIESST), is inversely proportional to the thermodynamic SCO temperature $T_{1/2}$ when similar materials are compared, according to Hauser's inverse energy gap law.[19] Internal structural rigidity within the molecular switching sites also tends to increase T(LIESST).[20] Since spin state trapping like the LIESST effect is a form of bistability, structure:function relationships governing T(LIESST) can help extend the effect to higher temperatures.[21]

Comparison of isomorphous SCO materials is particularly useful for determining structure:function relationships.[22-32] With that in mind, we recently reported a family of isomorphous solvate crystals [FeL_2]X$_2$·solv (L = 4-{*iso*propyl-sulfanyl}-2,6-di{pyrazol-1-yl}pyridine; **1X$_2$**·solv, Scheme 1), whose thermal spin state behaviours depend significantly on the solvent present.[30,31] A variety of spin state properties occurs in this system (Figure S1). These include abrupt and hysteretic spin transitions (**1[BF$_4$]$_2$**·MeCN, **1X$_2$**·H$_2$O and **1X$_2$**·sf); more gradual thermal SCO equilibria (**1[BF$_4$]$_2$**·MeNO$_2$, **1[BF$_4$]$_2$**·Me$_2$CO); and other examples that undergo SCO incompletely (**1[ClO$_4$]$_2$**·MeNO$_2$, **1[ClO$_4$]$_2$**·Me$_2$CO) or remain high-spin on cooling (**1[BF$_4$]$_2$**·EtCN, **1[ClO$_4$]$_2$**·MeCN). The larger

a. *School of Chemistry, University of Leeds, Woodhouse Lane, Leeds, UK LS2 9JT. E-mail: m.a.halcrow@leeds.ac.uk.*

b. *Institut de Physique de Rennes, Université de Rennes 1, UMR UR1-CNRS 6251, F-35000 Rennes, France. E-mail: eric.collet@univ-rennes1.fr*

c. *Institute of Chemical Sciences and Engineering, École Polytechnique Fédérale de Lausanne (EPFL), Laboratory for Computational Molecular Design, CH-1015 Lausanne, Switzerland. E-mail: sergi.vela@epfl.ch*

ClO_4^- anion consistently stabilises the high-spin form of these materials, while their SCO cooperativity appears to correlate with the solvent present where the comparison can be made.[31]
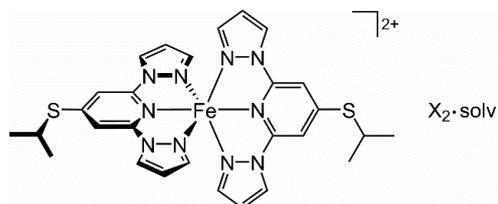
Scheme 1 Compound **1X₂·solv** (X^- = BF_4^- or ClO_4^-; solv = MeNO₂, MeCN, Me₂CO, H₂O or sf {solvent free}).

LIESST measurements on six **1X₂·solv** compounds yielded a surprising observation, that five samples cleanly follow the inverse energy gap law whereas the sixth example does not (Figure 1).[31] Photocrystallographic studies of three compounds showed the further complication, that **1[BF₄]₂·MeNO₂** undergoes two different symmetry-breaking phase changes before, and during, LIESST excitation at 15 K whereas **1[BF₄]₂·H₂O** and **1[BF₄]₂·MeCN** (the T(LIESST) outlier) do not. We proposed that the presence or absence of these phase changes in different samples might influence their T(LIESST) behaviour.[31]
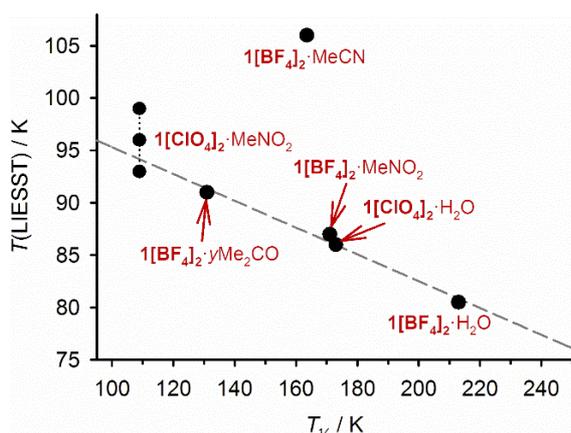
Figure 1 T(LIESST) vs $T_{½}$ plot for six **1X₂·solv** compounds.[31] Multiple T(LIESST) values were observed for **1[ClO₄]₂·MeNO₂**, which may reflect additional kinetic barriers to SCO that can occur at such low values of $T_{½}$.[31,33]

We now report a full investigation of the structural basis for thermal and light-induced SCO in this system. This includes more detailed crystallographic studies, clarifying the relationship between the spin states and disorder in these compounds. New photocrystallographic data for **1[BF₄]₂·MeNO₂** and the remaining compounds in Figure 1 are provided, and analysed for subtle changes in intermolecular interactions between their spin states. Computed spin state energies of the crystalline compounds also reproduce their thermal SCO temperatures, and give insight into the anomalous LIESST behaviour of **1[BF₄]₂·MeCN**. This comprises the most comprehensive structural study yet available, of thermal and light-induced SCO in isomorphous materials.

Results

The high-spin and low-spin forms of each SCO-active **1X₂·solv** material were crystallographically characterised in our earlier reports.[30,31] Each compound adopts the monoclinic $P2_1/c$ space group between 100-300 K in both spin states. Crystallographic disorder was noted in the anions, solvent and/or *iso*propylsulfanyl groups in different compounds, but no clear influence of that disorder on the SCO process was evident. To address this question, crystal structures of **1[BF₄]₂·solv** (solv = MeNO₂, yMe₂CO {y ≈ 0.75}, MeCN and H₂O) have now been redetermined at multiple temperatures. Each compound was measured at 5, 10 or 20 K intervals over a 110 or 120 K temperature range, chosen to span its spin transition. These measurements were performed in both cooling and warming temperature ramps for **1[BF₄]₂·MeCN**, to capture the thermal hysteresis in its spin transition.

The temperature dependence of the crystallographic spin states of each compound mostly mirrors their magnetic susceptibility data (Figure 2). An exception is **1[BF₄]₂·yMe₂CO** whose SCO has the same onset temperature on cooling in the diffractometer and SQUID magnetometer, but occurs less gradually and with a higher midpoint temperature in the crystallographic experiment. This may reflect the slower cooling rate employed in the X-ray structure determinations, where the crystal was poised for 2-3 hours at each temperature during the data collections.[33,34]

An unexpected structural temperature dependence was found, where the L tridentate ligand conformation consistently becomes less twisted at lower temperatures. That is expressed by the dihedral angle between the heterocyclic cores of the two L ligands (ϑ; Scheme S1), which increases linearly on cooling over the high-spin range of the crystals, at a rate between −0.010 and −0.016 degK⁻¹ (Figure S6). SCO in **1[BF₄]₂·solv** (solv = MeNO₂, MeCN and H₂O) is accompanied by a further increase in ϑ, which then shows a weaker negative temperature dependence in the low-spin crystals.[35] Conversely, the more gradual SCO in **1[BF₄]₂·yMe₂CO** reverses the temperature dependence of ϑ which then *increases* in cooling below $T_{½}$. The temperature dependence of ϑ in both spin states of each compound extends down to very low temperatures in the photocrystallographic experiments, by extrapolation from the higher temperature data (Figure S6). These effects will reflect the evolution of the lattice pressure experienced by the cations, upon anisotropic contraction of the monoclinic crystals on cooling. However, these changes at the periphery of the molecule have no detectable influence on the inner coordination sphere of the complex (Figure S6).

The crystal packing in **1[BF₄]₂·solv** is shown in Figure 3. The cations pack into bilayers parallel to (100), which are separated by sheets of anions and solvent spanning the crystallographic inversion centres. Four residues in the refinements are disordered to varying degrees at higher temperatures. These include the solvent, one BF_4^- ion and one *iso*propylsulfanyl residue which form the inter-bilayer space. The other BF_4^- ion lies within the cation bilayers, and is also always disordered at higher temperatures.[36]
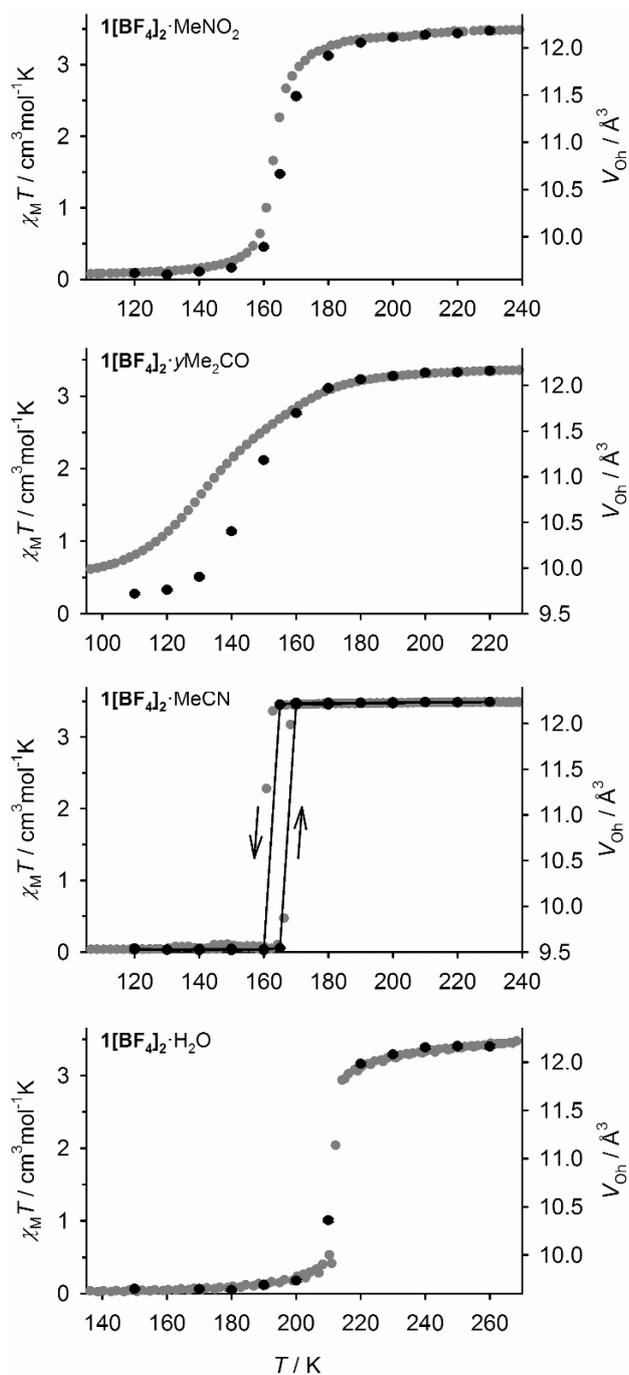
Figure 2 Comparison of the spin-transitions from magnetic susceptibility (grey) and crystallographic data (black) for four **1[BF$_4$]$_2$**·solv materials. V_{Oh} is the crystallographic volume of the FeN$_6$ coordination octahedron, a convenient measure of the Fe–N bond lengths at each temperature.[37,38] The crystallographic data for **1[BF$_4$]$_2$**·MeCN are linked by lines, to distinguish measurements in cooling and warming temperature ramps.

Disorder in the intra-bilayer anion is gradually quenched upon cooling. The approximate ordering temperature for this anion is near $T_{\frac{1}{2}}$ in **1[BF$_4$]$_2$**·yMe$_2$CO, but is unconnected to SCO in the other three solvates (Figures S10-S13).[36] The gradual SCO in **1[BF$_4$]$_2$**·yMe$_2$CO has little effect on the extensive disorder in the inter-bilayer space of that crystal (Figure S11), which is retained even at 20 K (see below). Conversely, the abrupt and hysteretic SCO in **1[BF$_4$]$_2$**·MeCN is clearly connected to the
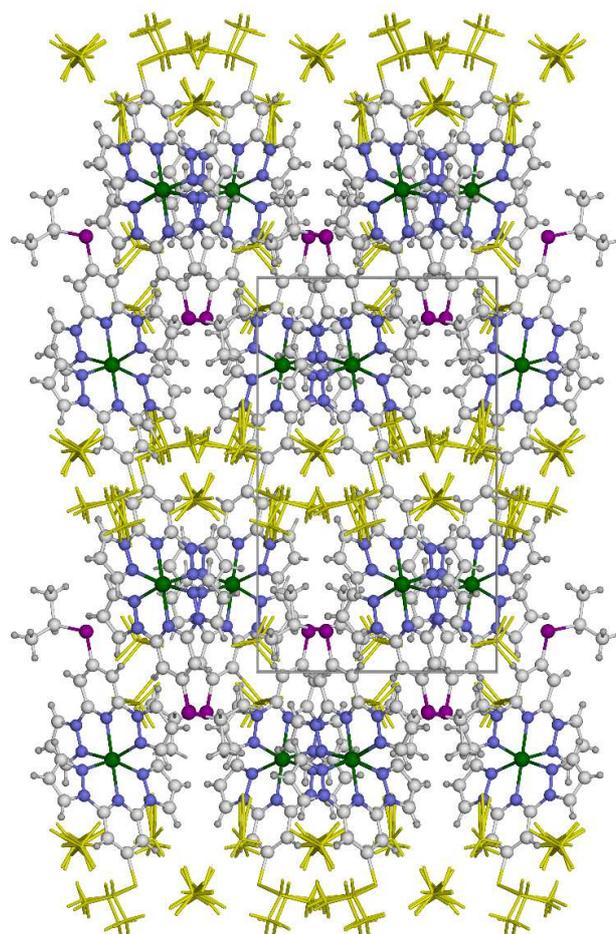
Figure 3 The packing diagram of **1[BF$_4$]$_2$**·MeCN at 165 K, in in its high-spin form. The view is parallel to the [001] vector, with the unit cell b axis horizontal. Disordered *iso*propylsulfanyl, anion and solvent residues are highlighted in yellow. Colour code for crystallographically ordered atoms: C, white; H, pale grey; Fe, green; N, blue; S, purple.

reversible onset of disorder in its mobile *iso*propylsulfanyl group and acetonitrile molecule (Figure S12). Hence the weak or strong SCO cooperativity in those crystals, at least, may correlate with their inter-bilayer disorder. The disorder in the other two solvates, and their SCO cooperativity, lie between these two extremes.

A previous photocrystallographic determination of low- and high-spin **1[BF$_4$]$_2$**·MeNO$_2$ at 15 K showed unexpectedly complicated behaviour,[31] which we have now characterised in more detail. This compound transforms on cooling between 80 and 75 K from its parent phase ($P2_1/c$, $Z = 4$; phase 1) to a new low-spin phase 2 ($P2_1/c$, $Z= 12$) characterised by a tripling of the unit cell b dimension (Figures S14-S15). A new analysis of this phase at 40 K was achieved during this study, which is essentially identical to the 15 K structure in our earlier report (Table S11).[31] Irradiation of this crystal caused a further transformation to a new high-spin phase 3 ($P2_1$, $Z = 4$), with a similar unit cell to phase 1 but lacking the crystallographic c glide plane. Rewarming the crystal under irradiation showed that phase 3 is retained on warming until 70±5 K, when it reconverts to phase 1 (Figure 4). This is a lower temperature than the high→low-spin thermal relaxation, which occurs
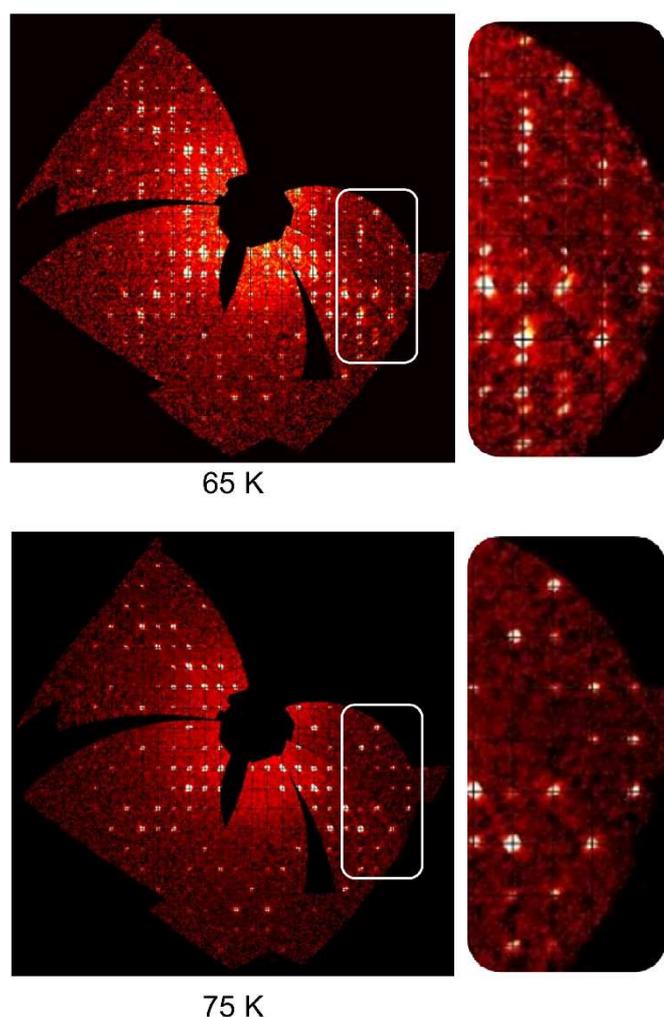
Figure 4 Diffraction images from **1[BF₄]₂·**MeNO₂ in the *hk*0 zone on warming from 65 to 75 K under continuous irradiation, and expansions of the highlighted region. The phase 3→phase 1 transformation is indicated by weak diffraction spots in the 65 K image, which are no longer present at 75 K. Images at other temperatures are shown in Figure S18.

spin states at 10-20 K. Conversely, low-spin **1[ClO₄]₂·**H₂O is crystallographically ordered at 10 K but irradiation of the crystal induces minor disorder in its inter-bilayer anion, along with the low→high-spin transition.[36] Isothermal SCO in **1[BF₄]₂·**MeCN at 85 K involves a 0.5 Å displacement and 31±1° rotation of the essentially linear acetonitrile molecule, which is crystallographically ordered at that temperature (Figure 5). The other crystals undergo much smaller rearrangements of their inter-bilayer residues between the spin states (Figure S21).
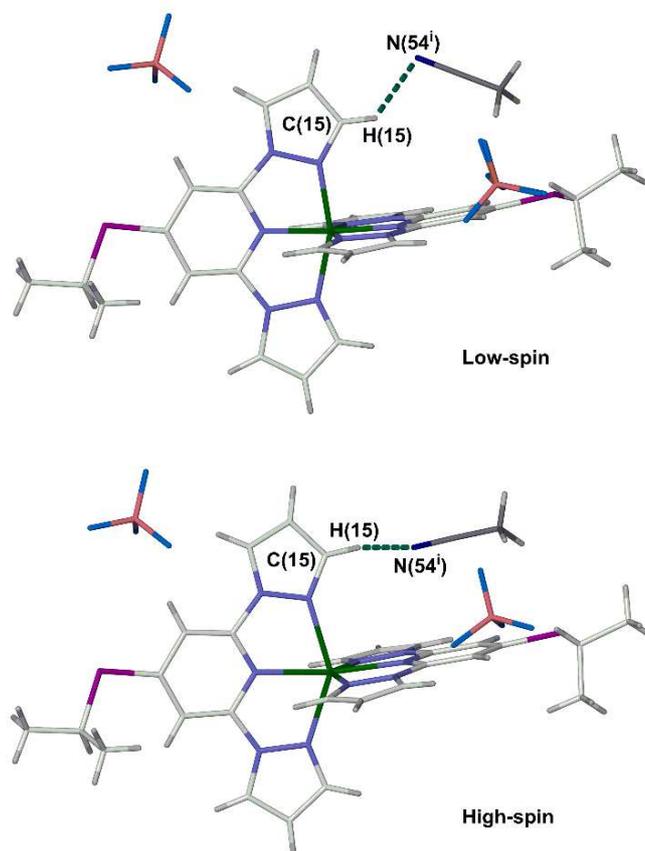
Figure 5 An intermolecular Van der Waals contact in **1[BF₄]₂·**MeCN at 85 K, which may couple the cation spin state to the solvent orientation during SCO [symmetry code: (i) 1–*x*, 1–*y*, 1–*z*]. Minor disorder of the inter-bilayer anion in the low-spin crystal is shown in the view. Colour code: C, white; H, pale grey; B, pink; F, cyan; Fe, green; N, blue; S, purple.

between 80 and 85 K in the crystal (Figure S17). Hence, unexpectedly, the phase 3→1 transformation does not coincide with the high→low-spin LIESST relaxation.

In contrast **1[BF₄]₂·**MeCN (at 85 K),[31] **1[BF₄]₂·***y*Me₂CO, **1[BF₄]₂·**H₂O,[31] **1[ClO₄]₂·**MeNO₂ and **1[ClO₄]₂·**H₂O (at 10-20 K) retain phase 1 before and after irradiation at these temperatures. Hence, **1[BF₄]₂·**MeNO₂ is the only material in Figure 1 to exhibit its complex phase behaviour. Consistent with its magnetic data (Figure S1), crystals of **1[ClO₄]₂·**MeNO₂ adopt a mixed high:low-spin population at 10 K, so the fully low-spin form of that compound could not be measured. As for the other solvates, however, **1[ClO₄]₂·**MeNO₂ was cleanly converted it to its pure high-spin form on irradiation at 10 K (Table S13).

Low-spin **1[BF₄]₂·***y*Me₂CO, **1[BF₄]₂·**MeCN,[31] **1[BF₄]₂·**H₂O[31] and **1[ClO₄]₂·**MeNO₂ all retain disorder in the inter-bilayer anion or solvent, at the lowest temperatures measured (Figure S19-S20). This disorder is quenched by the low→high-spin photoconversion in **1[BF₄]₂·**MeCN and **1[ClO₄]₂·**MeNO₂, but not in the other two crystals which are similarly disordered in both

Both **1[BF₄]₂·**MeCN[31] and **1[ClO₄]₂·**H₂O have the unusual property of a small, negative unit cell volume change (ΔV_{uc}) of –0.2 % during their isothermal low→high-spin photoexcitation. That correlates with the $\Delta V_{uc} \approx 0.1$ % observed for their thermal spin transitions, which is much smaller than the other compounds in the series (Figure S9).[30,31] In contrast **1[BF₄]₂·***y*Me₂CO, **1[BF₄]₂·**H₂O[31] and **1[ClO₄]₂·**MeNO₂ show more typical, positive ΔV_{uc} values of up to +0.55 % in the photocrystallographic experiment (Table S6).

Hirshfeld surfaces and interaction maps were calculated from all the isothermal photocrystallographic structures (Figures S22-S33).[39] Interaction maps of high-spin and low-spin **1[BF₄]₂·**MeCN at 165 K, and the thermally trapped high-spin crystal at 15 K, were also produced. Those three high-spin structures yielded essentially identical interaction maps

(allowing for the disordered solvent at 165 K), as did the two low-spin structures (Figures S22-S24). Interaction maps of high-spin and low-spin $1[BF_4]_2 \cdot H_2O$ were also produced at 20 K, and at temperatures either side of its abrupt thermal SCO at 213 K (Figures S25-S27). While these are complicated by disorder, strong similarities are also evident at the two temperatures for each spin state of that crystal. Hence, SCO has a much greater impact on the crystal packing in $1X_2 \cdot solv$ than the background contraction of the lattice on cooling.[40]

Neighbouring molecules in the cation bilayers interact through weak C–H...π contacts between their pyrazolyl rings, whose intermolecular H...C distances are shorter in the low-spin crystals. That reflects a 0.3-0.5 Å horizontal displacement of adjacent cations within the bilayers. The cations and anions interact through typical distributions of C–H...F or C–H...O distances, which don't change significantly during SCO. A weak anion...π interaction to the inter-bilayer BF_4^- or ClO_4^- ion is evident in $1[BF_4]_2 \cdot MeCN$ and $1[ClO_4]_2 \cdot MeNO_2$ (Figures S23 and S29), but not in the hydrate crystals where that anion participates in hydrogen bonding to the lattice water (Figures S26 and S32).

A C–H...Y (Y = N or O) Van der Waals contact between a complex pyrazolyl ring and the lattice solvent could play a role in coupling displacements of those residues during SCO (Figures 5 and S34-S36). All the solvates show this contact, which appears as a weak C–H...O hydrogen bond in Hirshfeld maps for $1[ClO_4]_2 \cdot MeNO_2$ and $1[ClO_4]_2 \cdot H_2O$ (Figures S30 and S33).[41] While this contact is 0.09-0.18 Å shorter in $1[BF_4]_2 \cdot MeCN$ than in the other solvates (Table S15), the significance of that is unclear.[42] More unambiguously, the contact is similarly short in both spin states of $1[BF_4]_2 \cdot MeCN$, but increases by up to 0.14 Å in the high-spin forms of the other solvates. Since it is retained in both spin states, that interaction may contribute to coupling the cation spin state and solvent orientation in $1[BF_4]_2 \cdot MeCN$.

Periodic DFT+U+D2 calculations were undertaken of the high- and low-spin states of four compounds in Figure 1. For comparison, two related compounds with available photocrystallographic data were also calculated: $[Fe(bpp)_2][BF_4]_2$ (2; bpp = 2,6-di{pyrazol-1-yl}pyridine)[43] and $[Fe(bpp^{CH2OH})_2][BF_4]_2$ (3; bpp^{CH2OH} = 4-hydroxymethyl-2,6-di{pyrazol-1-yl}pyridine; Scheme S3).[44] These two solvent-free compounds are crystallographically related, but in a different lattice structure from the $1X_2 \cdot solv$ series. The computations yield the solid state minima, whose energy corresponds to the electronic enthalpy (H_{elec}) contribution to the SCO transition. While they cannot account for thermally activated crystallographic disorder there is, at most, only minor disorder in the photocrystallographic structures of the compounds examined computationally (Figures S19-S21). A further discussion of the capabilities and limitations of the method is given in the ESI†.

The electronic energy change between the spin states in the crystal, ΔH_{elec}, is proportional to the overall enthalpy change during SCO which should correlate with $T_{\frac{1}{2}}$. This relationship holds well for the $1X_2 \cdot solv$ compounds, where ΔH_{elec} and $T_{\frac{1}{2}}$ both follow a reasonably linear correlation of $1[BF_4]_2 \cdot H_2O > 1[BF_4]_2 \cdot MeNO_2 \approx 1[ClO_4]_2 \cdot H_2O > 1[BF_4]_2 \cdot MeCN$ (Table 1, Figure 6). The reference compound 2 also has a significantly higher ΔH_{elec}, which is consistent with its higher $T_{\frac{1}{2}}$. The relationship fails for 3, however, whose ΔH_{elec} is similar to $1[BF_4]_2 \cdot H_2O$ despite its $T_{\frac{1}{2}}$ being more similar to 2. This implies the relationship between ΔH_{elec} and $T_{\frac{1}{2}}$ is different for 2 and 3 than for $1X_2 \cdot solv$. That should reflect their different lattice structure and lack of lattice solvent, which would significantly affect their vibrational enthalpy component, ΔH_{vib}.

The calculations capture the observed isothermal change in unit cell volume during SCO (ΔV_{uc}) in four of the six compounds
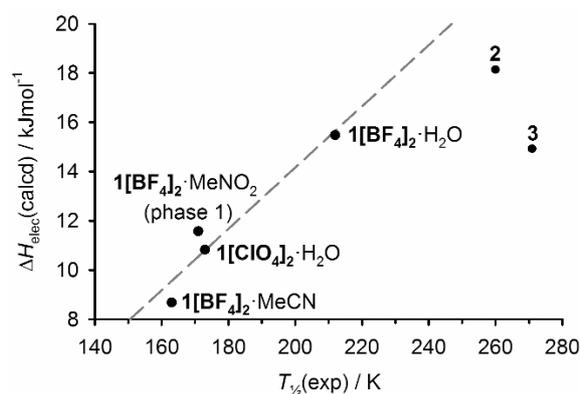
Figure 6 Correlation between the calculated enthalpy of spin-crossover (ΔH_{elec}) and the experimental SCO midpoint temperature $T_{\frac{1}{2}}$ for the compounds in the computational study. The dashed line shows the best fit regression for the four $1X_2 \cdot solv$ compounds.

Table 1 Computed electronic enthalpy differences between HS and LS minima of the compounds in this work, together with the average change in Fe–N bond length and % change in unit cell volume. Experimental structural data from the isothermal photocrystallographic studies of the compounds are also presented for comparison.

	$1[BF_4]_2 \cdot MeNO_2$ (phase 1)	$1[BF_4]_2 \cdot MeCN$	$1[BF_4]_2 \cdot H_2O$	$1[ClO_4]_2 \cdot H_2O$	2	3
ΔH_{elec} / kJmol^{-1}	11.57	8.68	15.48	10.82	18.14	14.92
$T_{\frac{1}{2}}$ / K	171	163	212	173	260	271
$T(LIESST)$ / K	87	106	81	86	81	70
Δd{Fe–N, calc} / Å	0.220	0.219	0.220	0.221	0.233	0.229
Δd{Fe–N, expt} / Å	0.209(18)[a]	0.216(5)	0.211(9)	0.210(6)	0.215(3)	0.200(4)
ΔV_{uc}{calc} / %	+0.53	+0.57	+0.29	−0.59	+2.98	+2.09
ΔV_{uc}{expt} / %	+1.31[a]	−0.20	+0.15	−0.19	+2.22	+1.57

[a]Normalised unit cell volume change for the phase 2→phase 3 transformation in this material

(Table 1 and Figure 7). One anomaly is **1[BF₄]₂·MeNO₂**, reflecting its phase 1→2→3 transformations which were not considered in the study. The other outlier is **1[BF₄]₂·MeCN** where a typical positive ΔV_{uc} is calculated, in contrast to the small negative value observed experimentally. Notably the other negative ΔV_{uc} exhibited by **1[ClO₄]₂·H₂O** *is* reproduced by the calculations.
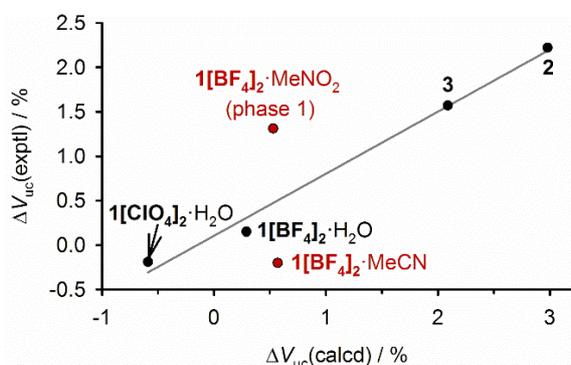
Figure 7 Computed and experimental ΔV_{uc} values for the compounds in Table 1 The grey line shows the best fit regression of the black data points on the graph.

Comparison of the observed and energy-minimised structures of **1[BF₄]₂·MeCN** shows significant differences in the disordered region of the asymmetric unit, which might account for these differences (Figure S37). In the low-spin form, the calculated orientation of the *iso*propyl group in the disordered region of the lattice is rotated by *ca* 12° compared to its experimental position at 85 K, while the solvent molecule is also displaced by 0.3 Å between the two models. In the high-spin calculation, that *iso*propyl residue is in better agreement with experiment, but the orientation of the MeCN molecule in the computed structure is rotated compared to the experimental one by 6.8° at 85 K, or by 6.6° at 15 K (Figure S37). Since these observations are unchanged upon cooling the crystal, the differences between computation and experiment for **1[BF₄]₂·MeCN** should not be caused by temperature effects.

The other minimised structures show better agreement between experiment and theory (Figures S38 and S39). The greatest discrepancy among the **1X₂·solv** compounds is the position of the inter-bilayer BF₄⁻ ion in high-spin **1[BF₄]₂·H₂O**, which is also shifted by 0.3 Å in the computed and experimental models. Since that anion is experimentally disordered, some disagreement between experiment and theory is reasonable in that case. Interestingly, the hydroxymethyl ligand substituents in **3** minimised to different conformations oriented towards different BF₄⁻ hydrogen-bond acceptors, in its two spin states. This conformational rearrangement doesn't occur experimentally during LIESST photoexcitation at 30 K, but is observed as crystallographic disorder at higher temperatures (Figure S40).[44]

The interaction energy terms contributing to ΔH_{elec} were deconvoluted into the individual energies of the cations, anions and solvent, which contribute to the conformation and ligand field of the molecules in the crystal; and, the intermolecular interaction energies between each of these components (Table S16). These data give insight into the contribution of each residue in the crystal to its spin state energies, which is discussed in the ESI†.

Discussion

Our new understanding of **1X₂·solv** can be compared to [Fe(pic)₃]Cl₂·ROH (pic = 2-{aminomethyl}pyridine; R = Me, Et, *n*-Pr, *i*-Pr, allyl or *t*Bu), which show widely differing spin state properties despite their structural similarity.[22] Recent computational studies have shown the magnitude of intermolecular interactions influences $T_{½}$ in these crystals, but has no effect on their SCO cooperativity.[25] Rather, the cooperativity differences may be governed by temperature-dependent disorder of the alcohol solvent, whose influence on the symmetry and spin state of the crystals differs significantly between the compounds.[23,24] That could be a simple mechanical effect between the lattice cavity occupied by the solvent and the differently shaped molecules held within it.

There is substantial evidence that the spin state properties of **1X₂·solv** are also governed by the solvent present. For example the cooperative, hysteretic thermal SCO in **1[BF₄]₂·MeCN** occurs simultaneously with ordering of the solvent and a ligand substituent in the inter-bilayer space (Figure S12). Conversely the most gradual SCO is found in **1[BF₄]₂·yMe₂CO**, where the same residues remain extensively disordered on cooling to 20 K (Figure S11). Moreover, the hydrate crystals **1[BF₄]₂·H₂O** and **1[ClO₄]₂·H₂O** are more similar to each other, than to the other solvates of each anion. That is clear in their abrupt, weakly hysteretic spin-transitions (Figures 2 and S1); the similar changes to their molecular and lattice structures during photoexcitation (Table S13, Figures S19-S21 and S38); and in their computed crystal energetics (Table S16).

Our photocrystallographic study provides a full set of structural data for the $T_{½}/T$(LIESST) correlation in Figure 1. Our former suggestion that T(LIESST) is influenced by the crystallographic symmetry-breaking shown by **1[BF₄]₂·MeNO₂** in the LIESST experiment, can now be ruled out.[31] On one hand, no other compound in Figure 1 exhibits those low-temperature phase changes. On the other, accurate measurement of the phase transition temperatures in **1[BF₄]₂·MeNO₂** has shown they occur 10-20 K below the onset of LIESST relaxation.

The calculations do not capture **1[BF₄]₂·MeCN** as an outlier from the inverse energy gap law in the LIESST experiment (Figure 1). Rather, they predict that **1[BF₄]₂·MeCN** should follow the same $\Delta H_{elec}/T_{½}$ correlation as the other **1X₂·solv** crystals (Figure 6). Moreover, the positive unit cell volume change (ΔV_{uc}) computed for its isothermal low→high-spin excitation disagrees with the negative ΔV_{uc} observed crystallographically (Figure 7). That suggests the minimised structure(s) of **1[BF₄]₂·MeCN** are not representative of the molecular arrangement during experiment. The largest discrepancy lies in the calculated orientations of the inter-bilayer *iso*propyl, anion and solvent moieties (Figures S37-S38). The mismatches in ΔH_{elec} and ΔV_{uc} both indicate the spin state properties of **1[BF₄]₂·MeCN** have, uniquely, been imperfectly reproduced by the calculations.

Since the calculations represent the thermodynamic minima for **1[BF₄]₂·MeCN**, this discrepancy between experiment and theory should have a kinetic origin. Hence, it is noteworthy that isothermal SCO in **1[BF₄]₂·MeCN** involves a much greater rearrangement of the inter-bilayer residues than for the other solvate crystals (Figures 5 and S21). Motion of these groups is more facile during thermal SCO around 165 K, where the solvent and neighbouring isopropyl group are disordered in the high-spin state (Figure S12), than under LIESST conditions where these groups are crystallographically ordered (Figure S20). That implies a higher lattice activation energy associated with solvent reorientation during LIESST relaxation, than for the thermal SCO. That could lead to a higher than expected *T*(LIESST) temperature, as observed.

Such a temperature-dependent lattice activation energy for SCO is not caused by significant changes to the crystal packing, according to the Hirshfeld analyses (Figures S22-S24). Rather, it should simply reflect the higher thermal phonon energy in the crystal at 165 K, resulting in a more deformable lattice during the thermal spin-transition.[45] Lattice softening on warming will also occur in other SCO materials, including the other **1X₂·solv** samples in Figure 1. However, LIESST relaxation should be less influenced by the lattice in those compounds, because of the smaller structural changes involved (Figure S20). Thus, the inverse energy law relationship between high-temperature SCO and low-temperature LIESST relaxation is obeyed by those materials, but not by **1[BF₄]₂·MeCN**.

Conclusions

This study provides the most detailed picture available, of the structural chemistry of isomorphous crystals exhibiting SCO under thermodynamic and kinetically controlled conditions (in the LIESST effect). The orientations and disorder of peripheral ligand substituents and solvent molecules strongly influence thermal SCO cooperativity in **1X₂·solv**. Our data have also detected an unexpected temperature dependence of the *L* ligand conformation in these compounds, occurring independently of SCO (Figure S6).[46] This highlights that reliable SCO structure:function relationships can only be inferred from crystal structures measured near the spin transition temperature.[12]

We also demonstrate, for the first time, that the same considerations can also affect *T*(LIESST). The deviation of **1[BF₄]₂·MeCN** from the inverse energy gap law, and its unusual unit cell contraction during low→high-spin photoexcitation, are not reproduced computationally. That implies those features are not linked to the thermodynamic spin state energies of the material, and instead have a kinetic origin. We attribute this to the reorientation of the acetonitrile molecule during the high→low-spin relaxation (Figure 5), which is much greater than in the other solvate crystals (Figure S21). When coupled to the highly anisotropic shape of the MeCN molecule, that solvent reorganisation should lead to a higher lattice activation energy for thermal SCO or LIESST relaxation compared to the other solvates (Figure 8). That has a greater impact on LIESST relaxation at low temperature, when that molecule is

crystallographically ordered, than in thermal SCO at higher temperatures which induces disorder in that region of the asymmetric unit (Figure S12).
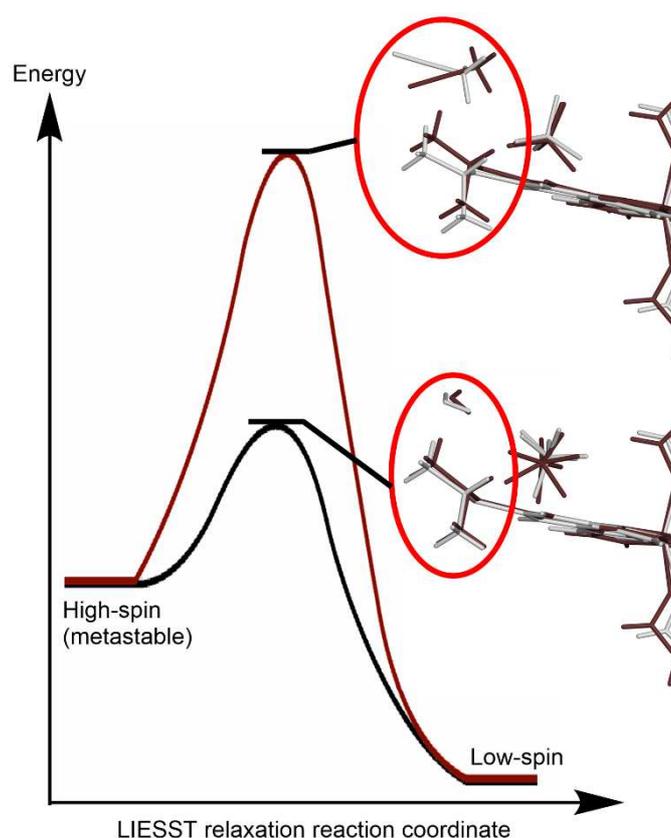
Figure 8 Diagram comparing the rearrangement of the inter-bilayer residues during the low-temperature isothermal high-spin (white)→low-spin (brown) transformation for **1[BF₄]₂·MeCN** (top) and **1[BF₄]₂·H₂O** (bottom), and showing their proposed effect on the activation energy for LIESST relaxation. Full overlays of these isothermal structure determinations are shown in Figure S21.

To conclude, the anomalous *T*(LIESST) in **1[BF₄]₂·MeCN** is a function of the anisotropic shape of the MeCN molecule. More generally, while the inverse energy gap law is well known to be influenced by the rigidity of the ligand sphere in a molecular complex,[20,47] the rigidity of the surrounding lattice also contributes to *T*(LIESST) in the **1X₂·solv** system. As well as informing the design of bistable SCO materials, this insight is relevant to wider studies of molecular dynamics in the crystalline state. These are of great current interest, following the recent development of ultrafast single crystal spectroscopies or diffraction methods.[17]

Experimental

Ligand *L* and the **1[BF₄]₂·solv** and **1[ClO₄]₂·solv** materials, and their single crystals, were prepared as previously described.[30,31] A crystal structure of ligand *L* is also included in the ESI†.

WARNING Although we encountered no issues in handling 1[ClO₄]₂ and its solvate crystals, metal/organic perchlorates are potentially explosive and should be handled with care in small quantities.

Diffraction data at temperatures above 100 K were collected with an Agilent Supernova dual-source diffractometer using monochromated Cu-K_α radiation (λ = 1.54184 Å). The diffractometer is fitted with an Oxford Cryosystems low-temperature device. Experimental details of the structure determinations are given in Tables S1-S5; every structure determination for each **1[BF$_4$]$_2$**·solv compound was obtained using the same crystal.

Crystallographic data below 100 K, before and after irradiation of the crystal, were measured using an Oxford Diffraction Xcalibur3 diffractometer and monochromated Mo-K_α radiation (λ = 0.71073 Å). The diffractometer was fitted with a Helijet Oxford Diffraction helium cryostat. A dataset from each crystal was first obtained in the dark, then the same crystal was irradiated with a 660nm *cw*-laser at *ca* 2mW laser power before recollection at the same temperature. Experimental details of these structure determinations are given in Table S6.

The structures were solved by isomorphous replacement based on their previously published structures,[30,31] and developed by full least-squares refinement on F^2 (*SHELXL97*[48]). Full crystallographic refinement details for each structure are given in the ESI†. Crystallographic figures were prepared using *X-SEED*,[49] V_{Oh} and other structural parameters were calculated using *Olex2*,[50] and Hirshfeld surfaces were calculated and analysed with *CrystalExplorer*.[51]

All computational energy evaluations were performed using the Quantum Espresso package (QE) Version 6.1,[52] using the PBE+*U*+D2 scheme, with a *U* parameter of 2.65 eV on the "*d*" orbitals of iron[53-55] and Grimme's D2 dispersion correction.[56] We have used the spin unrestricted formalism, Vanderbilt pseudopotentials[57] and a Γ-point sampling of the Brillouin zone. The computation of H_{elec} was done by successive variable-cell optimisations using a kinetic energy cut-off of 70 Ry, until the high-spin and low-spin solid-state minima were found.

The one- and two-body interaction terms in Table 3 were evaluated as in ref. 25. All one-body terms were computed as the sum of individual molecular energies, which were evaluated by means of separate single-point calculations at the solid-state minima, using a kinetic energy cutoff of 35 Ry, and the Makov-Payne energy correction when the molecules had a net charge (SCO and X).[58] All two-body terms were computed through single point evaluations of the solid state minima in which only one (for $\Delta H_{SCO-SCO}$, ΔH_{X-X} and $\Delta H_{solv-solv}$) or two (for ΔH_{SCO-X}, $\Delta H_{SCO-solv}$ and ΔH_{X-solv}) types of molecules are present in the unit cell. Then, the relevant one-body terms were subtracted to avoid double counting.

Conflicts of interest

There are no conflicts to declare.

Acknowledgements

Notes and references

1   P. Gütlich and H. A. Goodwin (eds.), Spin Crossover in Transition Metal Compounds I-III, *Top. Curr. Chem.* 2004, vols. 233-235.
2   M. A. Halcrow (ed), *Spin-crossover materials – properties and applications,* John Wiley & Sons, Chichester, UK, 2013, p. 568.
3   K. S. Kumar and M. Ruben, *Coord. Chem. Rev.*, 2017, **346**, 176–205; S. Rat, M. Piedrahita-Bello, L. Salmon, G. Molnár, P. Demont and A. Bousseksou, *Adv. Mater.*, 2018, **30**, 17003862.
4   For other recent reviews see: S. Brooker, *Chem. Soc. Rev.*, 2015, **44**, 2880–2892; O. Sato, *Nature Chem.*, 2016, **8**, 644–656; J. Zarembowitch, F. Varret, A. Hauser, J. A. Real and K. Boukheddaden, *C. R. Chimie*, 2018, **21**, 1056–1059; Z.-S. Yao, Z. Tang and J. Tao, *Chem. Commun.*, 2020, **56**, 2071–2086.
5   O. Kahn, J. Kröber and C. Jay, *Adv. Mater.*, 1992, **4**, 718–728.
6   See *eg* A. Rotaru, I. A. Gural'skiy, G. Molnár, L. Salmon, P. Demont and A. Bousseksou, *Chem. Commun.*, 2012, **48**, 4163–4165; H. Phan, S. M. Benjamin, E. Steven, J. S. Brooks and M. Shatruk, *Angew. Chem., Int. Ed.*, 2015, **54**, 823–827; H.-Y. Wang, J.-Y. Ge, C. Hua, C.-Q. Jiao, Y. Wu, C. F. Leong, D. M. D'Alessandro, T. Liu and J.-L. Zuo, *Angew. Chem., Int. Ed.*, 2017, **56**, 5465–5470; A. V. Kazakova, A. V. Tiunova, D. V. Korchagin, G. V. Shilov, E. B. Yagubskii, V. N. Zverev, S. C. Yang, J.-Y. Lin, J.-F. Lee, O. V. Maximova and A. N. Vasiliev, *Chem. Eur. J.*, 2019, **25**, 10204–10213.
7   See *eg* Y. Garcia, F. Robert, A. D. Naik, G. Zhou, B. Tinant, K. Robeyns, S. Michotte and L. Piraux, *J. Am. Chem. Soc.*, 2011, **133**, 15850–15853; S. Titos-Padilla, J. M. Herrera, X.-W. Chen, J. J. Delgado and E. Colacio, *Angew. Chem., Int. Ed.*, 2011, **50**, 3290–3293; C.-F. Wang, R.-F. Li, X.-Y. Chen, R.-J. Wei, L.-S. Zheng and J. Tao, *Angew. Chem., Int. Ed.*, 2015, **54**, 1574–1577; A. Santoro, L. J. Kershaw Cook, R. Kulmaczewski, S. A. Barrett, O. Cespedes and M. A. Halcrow, *Inorg. Chem.*, 2015, **54**, 682–693; C. Lochenie, K. Schötz, F. Panzer, H. Kurz, B. Maier, F. Puchtler, S. Agarwal, A. Köhler and B. Weber, *J. Am. Chem. Soc.*, 2018, **140**, 700–709; J.-L. Wang, Q. Liu, Y.-S. Meng, X. Liu, H. Zheng, Q. Shi, C.-Y. Duan and T. Liu, *Chem. Sci.*, 2018, **9**, 2892–2897.
8   See *eg* M. Nakano, G. Matsubayashi and T. Matsuo, *Phys. Rev. B: Condens. Matter Mater. Phys.*, 2002, **66**, 212412.; V. Jornet-Mollá, Y. Duan, C. Giménez-Saiz, Y.-Y. Tang, P.-F. Li, F. M. Romero and R.-G. Xiong, *Angew. Chem. Int. Ed.*, 2017, **56**, 14052–14056; H. Zheng, Y.-S. Meng, G.-L. Zhou, C.-Y. Duan, O. Sato, S. Hayami, Y. Luo and T. Liu, *Angew. Chem., Int. Ed.*, 2018, **57**, 8468–8472; S. Rat, M. Piedrahita-Bello, L. Salmon, G. Molnár, P. Demont, A. Bousseksou, *Adv. Mater.*, 2018, **30**, 1705275.
9   R. Akiyoshi, Y. Hirota, D. Kosumi, M. Tsutsumi, M. Nakamura, L. F. Lindoy and S. Hayami, *Chem. Sci.*, 2019, **10**, 5843–5848.
10 A. B. Gaspar and M. Seredyuk, *Coord. Chem. Rev.*, 2014, **268**, 41–58.
11 See *eg* M. D. Manrique-Juárez, S. Rat, L. Salmon, G. Molnár, C. M. Quintero, L. Nicu, H. J. Shepherd and A. Bousseksou, *Coord. Chem. Rev.*, 2016, **308**, 395–408; A. I. Vicente, A. Joseph, L. P. Ferreira, M. de Deus Carvalho, V. H. N. Rodrigues, M. Duttine, H. P. Diogo, M. E. Minas da Piedade, M. J. Calhorda and P. N. Martinho, *Chem. Sci.*, 2016, **7**, 4251–4258; M. D. Manrique-Juárez, F. Mathieu, V. Shalabaeva, J. Cacheux, S. Rat, L. Nicu, T. Leïchlé, L. Salmon, G. Molnár and A. Bousseksou, *Angew. Chem., Int. Ed.*, 2017, **56**, 8074–8078; M. D. Manrique-Juárez, F. Mathieu, A. Laborde, S. Rat, V. Shalabaeva, P. Demont, P. Thomas, L. Salmon, T. Leïchlé, L. Nicu, G. Molnár and A. Bousseksou, *Adv. Funct. Mater.*, 2018, **28**, 1801970.
12 M. A. Halcrow, *Chem. Soc. Rev.*, 2011, **40**, 4119–4142.
13 S. Rat, M. Piedrahita-Bello, L. Salmon, G. Molnár, P. Demont and A. Bousseksou, *Adv. Mater.*, 2018, **30**, 1705275; R. Torres-Cavanillas, R. Sanchis-Gual, J. Dugay, M. Coronado-Puchau, M.

Giménez-Marqués and E. Coronado, *Adv. Mater.*, 2019, **31**, 1900039.

14 D. Gentili, N. Demitri, B. Schäfer, F. Liscio, I. Bergenti, G. Ruani, M. Ruben and M. Cavallini, *J. Mater. Chem. C,* 2015, **3**, 7836–7844; R. G. Miller and S. Brooker, *Chem. Sci.*, 2016, **7**, 2501–2505; Y. Guo, S. Xue, M. M. Dîrtu and Y. Garcia, *J. Mater. Chem. C,* 2018, **6**, 3895–3900; K. Boukheddaden, M. H. Ritti, G. Bouchez, M. Sy, M. M. Dîrtu, M. Parlier, J. Linares and Y. Garcia, *J. Phys. Chem. C*, 2018, **122**, 7597–7604; E. Resines-Urien, E. Burzurí, E. Fernandez-Bartolome, M. A. G. García-Tuñón, P. de la Presa, R. Poloni, S. J. Teat and J. S. Costa, *Chem. Sci.*, 2019, **10**, 6612–6616.

15 P. J. von Ranke, B. P. Alho, R. M. Ribas, E. P. Nobrega, A. Caldas, V. S. R. de Sousa, M. V. Colaço, L. F. Marques, D. L. Rocco and P. O. Ribeiro, *Phys. Rev. B,* 2018, **98**, 224408; S. P. Vallone, A. N. Tantillo, A. M. dos Santos, J. Molaison, R. Kulmaczewski, A. Chapoy, P. Ahmadi, M. A. Halcrow and K. G. Sandeman, *Adv. Mater.*, 2019, **31**, 1807334; K. Ridier, Y. Zhang, M. Piedrahita-Bello, C. M. Quintero, L. Salmon, G. Molnár, C. Bergaud and A. Bousseksou, *Adv. Mater.*, 2020, **32**, 2000987.

16 S. Hayami, S. M. Holmes and M. A. Halcrow, *J. Mater. Chem. C,* 2015, **3**, 7775–7778.

17 R. Bertoni, M. Lorenc, A. Tissot, M.-L. Boillot and E. Collet, *Coord. Chem. Rev.*, 2015, **282–283**, 66–76; M. Chergui and E. Collet, *Chem. Rev.*, 2017, **117**, 11025–11065.

18 S. Decurtins, P. Gütlich, C. P. Köhler, H. Spiering and A. Hauser, *Chem. Phys. Lett.*, 1984, **105**, 1–4; S. Decurtins, P. Gütlich, C. P. Köhler and H. Spiering, *J. Chem. Soc., Chem. Commun.*, 1985, 430–432.

19 A. Hauser, J. Jeftić, H. Romstedt, R. Hinek and H. Spiering, *Coord. Chem. Rev.*, 1999, **190–192**, 471–491.

20 J.-F. Létard, *J. Mater. Chem.*, 2006, **16**, 2550–2559; G. Chastanet, C. Desplanches, C. Baldé, P. Rosa, M. Marchivie and P. Guionneau, *Chem. Sq.*, 2018, **2**, 2.

21 V. Gómez, C. Sáenz de Pipaón, P. Maldonado-Illescas, J. C. Waerenborgh, E. Martin, J. Benet-Buchholz and J. R. Galán-Mascarós, *J. Am. Chem. Soc.*, 2015, **137**, 11924–11927; A. Moneo-Corcuera, D. Nieto-Castro, C. Sáenz de Pipaón, V. Gómez, P. Maldonado-Illescas and J. R. Galán-Mascarós, *Dalton Trans.*, 2018, **47**, 11895–11902.

22 M. Hostettler, K. W. Törnroos, D. Chernyshov, B. Vangdal and H.-B. Bürgi, *Angew. Chem., Int. Ed.*, 2004, **43**, 4589–4594.

23 D. Chernyshov, M. Hostettler, K. W. Törnroos and H.-B. Bürgi, *Angew. Chem., Int. Ed.*, 2003, **42**, 3825–3830; D. Chernyshov, N. Klinduhov, K. W. Törnroos, M. Hostettler, B. Vangdal and H.-B. Bürgi, *Phys. Rev. B: Condens. Matter Mater. Phys.,* 2007, **76**, 014406; S. Vela and H. Paulsen, *Inorg. Chem.*, 2018, **57**, 9478–9488.

24 K. W. Törnroos, M. Hostettler, D. Chernyshov, B. Vangdal and H.-B. Bürgi, *Chem. Eur. J.*, 2006, **12**, 6207–6215; D. Chernyshov, B. Vangdal, K. W. Törnroos and H.-B. Bürgi, *New J. Chem.*, 2009, **33**, 1277–1282.

25 S. Vela and H. Paulsen, *Dalton Trans.*, 2019, **48**, 1237–1245.

26 P. Guionneau, J.-F. Létard, D. S. Yufit, D. Chasseau, G. Bravic, A. E. Goeta, J. A. K. Howard and O. Kahn, *J. Mater. Chem.*, 1999, **9**, 985–994; M. Marchivie, P. Guionneau, J.-F. Létard and D. Chasseau, *Acta Cryst. Sect. B: Struct. Sci.*, 2003, **59**, 479–486.

27 M. Yamada, H. Hagiwara, H. Torigoe, N. Matsumoto, M. Kojima, F. Dahan, J.-P. Tuchagues, N. Re and S. Iijima, *Chem. Eur. J.*, 2006, **12**, 4536–4549; T. Sato, K. Nishi, S. Iijima, M. Kojima and N. Matsumoto, *Inorg. Chem.*, 2009, **48**, 7211–7229.

28 I. Nemec, R. Herchel and Z. Trávníček, *Dalton Trans.*, 2015, **44**, 4474–4484.

29 B. Li, R.-J. Wei, J. Tao, R.-B. Huang, L.-S. Zheng and Z. Zheng, *J. Am. Chem. Soc.*, 2010, **132**, 1558–1566; R.-J. Wei, J. Tao, R.-B. Huang and L.-S. Zheng, *Inorg. Chem.*, 2011, **50**, 8553–8564.

30 L. J. Kershaw Cook, R. Kulmaczewski, O. Cespedes and M. A. Halcrow, *Chem. Eur. J.*, 2016, **22**, 1789–1799.

31 R. Kulmaczewski, E. Trzop, L. J. Kershaw Cook, E. Collet, G. Chastanet and M. A. Halcrow, *Chem. Commun.*, 2017, **53**, 13268–13271.

32 W. Phonsri, P. Harding, L. Liu, S. G. Telfer, K. S. Murray, B. Moubaraki, T. M. Ross, G. N. L. Jameson and D. J. Harding, *Chem. Sci.*, 2017, **8**, 3949–3959.

33 G. Ritter, E. König, W. Irler and H. A. Goodwin, *Inorg. Chem.*, 1978, **17**, 224–228; V. A. Money, C. Carbonera, J. Elhaïk, M. A. Halcrow, J. A. K. Howard and J.-F. Létard, *Chem. Eur. J.*, 2007, **13**, 5503–5514; J.-F. Létard, S. Asthana, H. J. Shepherd, P. Guionneau, A. E. Goeta, N. Suemura, R. Ishikawa and S. Kaisaki, *Chem. Eur. J.*, 2012, **18**, 5924–5934; Y. S. Ye, X. Q. Chen, Y. D. Cai, B. Fei, P. Dechambenoit, M. Rouzières, C. Mathonière, R. Clérac and X. Bao, *Angew. Chem., Int. Ed.*, 2019, **58**, 18888–18891; Y.-C. Chen, Y. Meng, Y.-J. Dong, X.-W. Song, G.-Z. Huang, C.-L. Zhang, Z.-P. Ni, J. Navařík, O. Malina, R. Zbořil and M.-L. Tong, *Chem. Sci.*, 2020, **11**, 3281–3289.

34 P. Guionneau, F. LeGac, S. Lakhoufi, A. Kaiba, D. Chasseau, J.-F. Létard, P. Négrier, D. Mondieig, J. A. K. Howard and J.-M. Léger, *J. Phys.: Condens. Matter*, 2007, **19**, 326211.

35 The esds on θ lie between 0.02-0.04° (Tables S7-S10). While differences in θ at 10 K temperature intervals are barely statistically significant, the linear trends over a 50-100 K window are well outside the error on the measurement.

36 Anions were modelled as disordered if two of their F or O atoms exhibited $U_{iso} \geq 0.07$ above 100 K, or $U_{iso} \geq 0.04$ in the photocrystallographic studies at helium temperatures. The same criteria were used for peripheral atoms in the solvent molecules, and for *iso*propylmethyl groups. In practise the anion displacement ellipsoids in **1[BF₄]₂**·solv decrease slowly on cooling over the temperature range of the experiment. Hence, a change from an ordered to a disordered refinement at 10 K lower temperature does not imply an abrupt quenching in those anions. Crystallographic ordering of the disordered solvent and/or *iso*propyl residues occurs more abruptly in conjunction with their SCO, where this is observed (Figures 10-13).

37 P. Guionneau, M. Marchivie, G. Bravic, J.-F. Létard and D. Chasseau, *Top. Curr. Chem.*, 2004, **234**, 97–128.

38 In compounds related to **1X₂**·solv, V_{Oh} is typically <10 Å³ in the low-spin state and ≥11.5 Å³ in their high-spin form.[59]

39 J. J. McKinnon, M. A. Spackman and A. S. Mitchell, *Acta Cryst. Sect. B: Struct. Sci.*, 2004, **60**, 627–668; J. J. McKinnon, D. Jayatilaka and M. A. Spackman, *Chem. Commun.*, 2007, 3814–3816; M. A. Spackman and D. Jayatilaka, *CrystEngComm*, 2009, **11**, 19–32.

40 P. Guionneau, M. Marchivie, G. Bravic, J.-F. Létard and D. Chasseau, *J. Mater. Chem.*, 2002, **12**, 2546–2551.

41 G. Desiraju and T. Steiner, *The Weak Hydrogen Bond: In Structural Chemistry and Biology.* Oxford University Press: Oxford, UK, 2001, p. 528.

42 The Pauling Van der Waals radius of a CH$_x$ group is 2.0 Å, and of an aromatic ring is 1.7 Å.[60] In practise the radius of the C–H groups in the C–H...Y interactions (Figures S33-S35) will lie between those limiting values, depending on the relative positions of the C–H and Y moieties. Hence, while this distance is shortest for **1[BF₄]₂**·MeCN it is unclear if that implies this contact is stronger for that crystal, or simply reflects the positioning of the solvent molecule over the adjacent pyrazolyl ring.

43 V. A. Money, I. Radosavljevic Evans, M. A. Halcrow, A. E. Goeta and J. A. K. Howard, *Chem. Commun.*, 2003, 158–159.

44 V. A. Money, J. Elhaïk, M. A. Halcrow and J. A. K. Howard, *Dalton Trans.*, 2004, 1516–1518.

45 A. Palii, S. Ostrovsky, O. Reu, B. Tsukerblat, S. Decurtins, S.-X. Liu and S. Klokishner, *J. Chem. Phys.*, 2015, **143**, 084502; E. Collet, G. Azzolina, T. Ichii, L. Guerin, R. Bertoni, A. Moreac, M.

Cammarata, N. Daro, G. Chastanet, J. Kubicki, K. Tanaka and S. F. Matar, *Eur. Phys. J. B: Cond. Matter Compl. Syst.,* 2019, **92**, 12.

46 C. M. Pask, S. Greatorex, R. Kulmaczewski, A. Baldansuren, E. J. L. McInnes, F. Bamiduro, M. Yamada, N. Yoshinari, T. Konno and M. A. Halcrow, *Chem. Eur. J.*, 2020, **26**, 4833–4841.

47 J.-F. Létard, P. Guionneau, O. Nguyen, J. S. Costa, S. Marcén, G. Chastanet, M. Marchivie and L. Goux-Capes, *Chem. Eur. J.*, 2005, **11**, 4582–4589.

48 G. M. Sheldrick, *Acta Cryst. Sect. C.: Struct. Chem.*, 2015, **71**, 3–8.

49 L. J. Barbour, *J. Supramol. Chem.*, 2001, **1**, 189–191.

50 O. V. Dolomanov, L. J. Bourhis, R. J. Gildea, J. A. K. Howard and H. Puschmann, *J. Appl. Cryst.*, 2009, **42**, 339–341.

51 M. J. Turner, J. J. McKinnon, S. K. Wolff, D. J. Grimwood, P. R. Spackman, D. Jayatilaka and M. A. Spackman, *CrystalExplorer17*. University of Western Australia, 2017. http://hirshfeldsurface.net.

52 P. Giannozzi, S. Baroni, N. Bonini, M. Calandra, R. Car, C. Cavazzoni, D. Ceresoli, G. L. Chiarotti, M. Cococcioni, I. Dabo, A. D. Corso, S. de Gironcoli, S. Fabris, G. Fratesi, R. Gebauer, U. Gerstmann, C. Gougoussis, A. Kokalj, M. Lazzeri, L. Martin-Samos, N. Marzari, F. Mauri, R. Mazzarello, S. Paolini, A. Pasquarello, L. Paulatto, C. Sbraccia, S. Scandolo, G. Sclauzero, A. P. Seitsonen, A. Smogunov, P. Umari and R. M. Wentzcovitch, *J. Phys.: Condens. Matter*, 2009, **21**, 395502.

53 A. I. Liechtenstein, V. I. Anisimov and J. Zaanen, *Phys. Rev. B: Condens. Matter Mater. Phys.,* 1995, **52**, R5467–R5470.

54 S. L. Dudarev, G. A. Botton, S. Y. Savrasov, C. J. Humphreys and A. P. Sutton, *Phys. Rev. B: Condens. Matter Mater. Phys.*, 1998, **57**, 1505–1509.

55 S. Vela, M. Fumanal, J. Ribas-Arino and V. Robert, *Phys. Chem. Chem. Phys.*, 2015, **17**, 16306–16314.

56 S. Grimme, *J. Comput. Chem.*, 2006, **27**, 1787–1799.

57 D. Vanderbilt, *Phys. Rev. B: Condens. Matter Mater. Phys.,* 1990, **41**, 7892–7895.

58 G. Makov and M. C. Payne, *Phys. Rev. B: Condens. Matter Mater. Phys.,* 1995, **51**, 4014–4022.

59 I. Capel Berdiell, R. Kulmaczewski and M. A. Halcrow, *Inorg. Chem.*, 2017, **56**, 8817–8828.

60 A. J. Gordon and R. A. Ford, *The Chemists Companion – a Handbook of Practical Data, Techniques and References*, John Wiley, Chichester, 1972, pp. 109.